# SSM/I Observations of ERICA IOP 4 Marine Cyclone: A Comparison with In Situ Observations and Model Simulation

SIMON W. CHANG

*Naval Research Laboratory, Washington, D.C.*

RANDALL J. ALLISS AND SETHU RAMAN

*Department of Marine, Earth and Atmospheric Sciences, North Carolina State University, Raleigh, North Carolina*

JAINN-JONG SHI

*Science Applications International Corporation, McLean, Virginia*

(Manuscript received 6 October 1992, in final form 3 March 1993)

ABSTRACT

Fields of rainfall rates, integrated water vapor (IWV), and marine surface wind speeds retrieved by the Special Sensor Microwave/Imager (SSM/I) during the intensive observational period 4 on 4 January 1989 of the Experiment on Rapidly Intensifying Cyclones over the Atlantic (ERICA) were analyzed. Subjectively analyzed and model-simulated frontal structures were used to examine the spatial relationship of the SSM/I observed fields to the rapidly intensifying storm and the associated fronts. Qualitative and quantitative comparisons of SSM/I retrievals with GOES imagery, conventional observations, and results produced from the Naval Research Laboratory's (NRL) limited-area numerical model were also made.

SSM/I rainfall was found along the cold and warm fronts, with heavy precipitation within frontal bands. The spatial pattern and characteristics of SSM/I precipitation closely resembled those simulated by the model. Both the warm and the cold front were found to be located near the area of the strongest gradient in IWV. In the warm sector, areas of IWV greater than 40 mm were found, an amount supported by model simulations. Both SSM/I rain rate and IWV distribution were found to be useful in locating the cold and warm fronts. There was good agreement on the relationship of frontal locations to the precipitation patterns and IWV gradients. Most of the high-wind area near the storm center was obscured by clouds for marine surface wind retrieval. SSM/I-retrieved marine surface winds outside the cloud shield (flag 0) were compared to ship- and buoy-reported winds. It was found that the retrieved wind estimates were within 0–3 m $s^{-1}$ of in situ observation over areas of slow wind shifts. The errors became larger in regions of rapid wind shifts.

## 1. Introduction

Since first deployed in earth orbit in the 1960s, meteorological satellites have been beneficial in tracking the course and development of maritime extratropical cyclones. Visible and infrared satellite imageries have aided forecasters in the analysis of these storms over the data-sparse oceans.

Over the past 15 years, sensors responsive to the upwelling microwave radiation have been launched aboard polar orbiting satellites. Microwave remote sensing has provided significant improvements in quantitative measurements of atmospheric variables such as integrated water vapor, rainfall rates, and marine surface wind speeds. Because the ocean has a relatively low and uniform emissivity compared with land in the microwave region, the ocean becomes an excellent background for measuring these parameters that are associated with extratropical cyclones. Meteorological parameters have been successfully obtained from the Scanning Multichannel Microwave Radiometer (SMMR) aboard the Seasat and *Nimbus-7* satellites, and the Electrically Scanning Microwave Radiometer (ESMR) aboard the *Nimbus-6* and *-7* satellites, and have been useful in the research of tropical and extratropical cyclones (Rodgers and Adler 1981; McMurdie and Katsaros 1985; Katsaros and Lewis 1986; McMurdie et al. 1987).

More recently, microwave remote sensing of tropical and extratropical systems has been improved via data collected from the Special Sensor Microwave/Imager (SSM/I) that flies aboard the Defense Meteorological Satellite Program (DMSP) satellites. Compared to the SMMR and ESMR sensors, the polar orbiting SSM/I operates continuously, providing much better sampling of marine cyclones. The SSM/I swath width is ap-

*Corresponding author address:* Dr. Simon W. Chang, Naval Research Laboratory, Code 7220, Washington, DC 20375-5000.

proximately 1400 km, which is nearly double that of SMMR. Relatively high-resolution (~25 km) products are routinely being provided by SSM/I. Good resolution is required when studying the intense mesoscale precipitation patterns that are observed in marine cyclones.

This paper presents an analysis of SSM/I-observed fields of an explosive midlatitude cyclone that developed on 4 January 1989 during the intensive observational period (IOP) 4 of the Experiment on Rapidly Intensifying Cyclones over the Atlantic (ERICA). SSM/I-derived rainfall rates, integrated water vapor (IWV), and marine surface wind speeds are all used to study the storm structure. Comparisons of SSM/I-retrieved marine surface winds with in situ ship and buoy reports will also be presented. Quantitative comparison of SSM/I-retrieved rain rates and IWV with independent observations is difficult; therefore, they will be compared with realistically simulated results produced by a limited-area model initialized with the National Meteorological Center Regional Analysis and Forecast System (NMCRAFS) analysis. Comparison of SSM/I-retrieved and model-generated fields has been conducted before, mainly for verification of numerical prediction models (e.g., Raustein et al. 1991; Pudykiewicz et al. 1992). In this study, ERICA IOP 4 frontal positions based on SSM/I retrieval and model results will be compared with subjectively analyzed positions of Neiman and Shapiro (1993). The motivation of this work is 1) to analyze ERICA IOP 4 marine cyclones based on SSM/I observations, 2) to provide a mutual validation of the SSM/I-observed quantities and independently obtained, realistic numerical model simulations, and 3) to prepare for the eventual use of SSM/I data in initializing numerical models in order to improve the forecast of intense cyclones over data-sparse oceans.

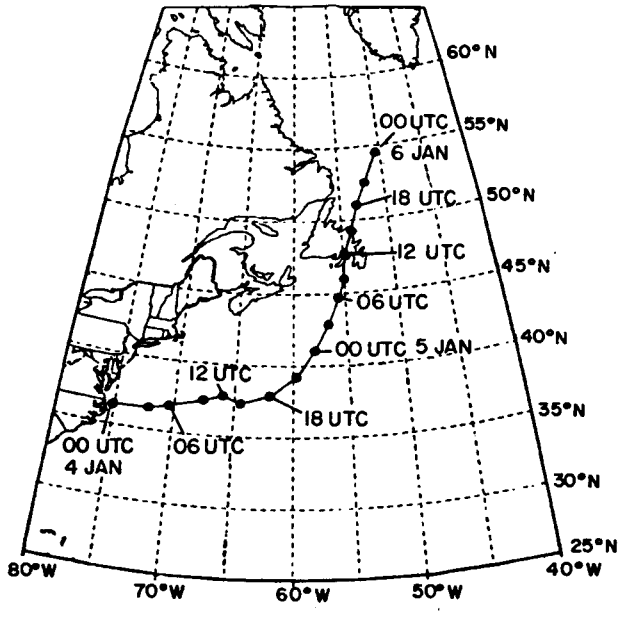


FIG. 1. The 3-h storm track of ERICA IOP 4 cyclone. Times are labeled every 6 h from 0000 UTC 4 January to 0000 UTC 6 January 1989.

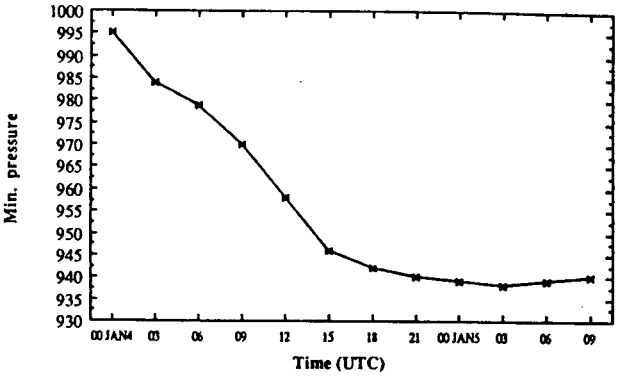


FIG. 2. Central pressure (mb) evolution from 0000 UTC 4 January to 0000 UTC 5 January. A deepening rate of 24 mb (6 h)$^{-1}$ was estimated to have occurred between 0900 and 1500 UTC.

## 2. Synoptic overview of ERICA IOP-4

ERICA field summary, NMC surface analysis, and surface analyses by Sanders (1993, personal communication), Neiman and Shapiro (1993), and Neiman et al. (1993), as well as airborne radar observations of Wakimoto et al. (1992), indicated that a cyclone developed rapidly and tracked east and northeast over the western North Atlantic Ocean during ERICA IOP 4. Figure 1 shows the storm track from the ERICA field summary. The initial stages of development were characterized by an incipient marine cyclone off Cape Hatteras, North Carolina. A coastal trough and front extended southwestward from the cyclone center, separating warm, moist air over the Gulf Stream from cooler and drier continental air situated over the coastal plain.

The low developed in response to a vigorous upper-level short wave that crossed the United States east coast at approximately 0000 UTC 4 January. Cyclogenesis commenced beneath difluent frontolytic 500-mb flow and strong 700-mb ascent with vertical velocities greater than 6 cm s$^{-1}$ after the approaching upper-level jet streak became vertically in phase with the surface cyclone (Neiman et al. 1993). Over the next 24 h the cyclone deepened from 996 mb at 0000 UTC 4 January to 938 mb at 0000 UTC 5 January (Fig. 2, ERICA field summary). The end of the rapid deepening phase occurred around 1800 UTC 4 January when a central pressure of 942 mb was analyzed. The storm produced a line of intense thunderstorms in advance of the cold front. A strong northwesterly flow of cold air to the rear of the storm produced the dramatic cloud street pattern seen in the imagery. The tight cloud band that nearly encompassed a small "eye" feature marked the location of lowest pressure at this time.

This eyelike feature may have been the result of strong mesoscale convection near the center of the storm during the period of rapid intensification. For additional detailed synoptic analyses, GOES imagery, and airborne radar observations of the ERICA IOP 4 cyclone, readers are referred to Wakimoto et al. (1992), Neiman and Shapiro (1993), Neiman et al. (1993), Sanders (1989), and Sanders (1993, personal communication).

SSM/I-retrieved fields and model-simulated fields will be analyzed in relationship to the unique frontal structure of the ERICA IOP 4 storm in this study. The frontal positions at 0000, 0600, 1200, and 1800 UTC on 4 January and 0000 UTC on 5 January are plotted in Fig. 3. During the period of interest between 0000 UTC 4 January and 0000 UTC 5 January, DMSP F-8 with SSM/I flew over the ERICA IOP 4 storm at 0000, 0930, and 2200 UTC 4 January. To facilitate the comparison with synoptic analysis, the frontal positions of Neiman et al. (1993) were linearly interpolated in time to produce the front structure at 0930 and 2200 UTC (Fig. 4). We should note that these frontal positions are based on eyeball interpolation of Neiman et al. and are not supported by any observations.

## 3. SSM/I: Sensor and algorithm

The microwave sensor SSM/I, from which observations were made for this study, was launched in June 1987. This radiometer has seven channels at 19.35, 22.235, 37.0, and 85.5 GHz, all with both vertical and horizontal polarizations except for the 22.235-GHz channel, which has only vertical polarization. The SSM/I measures upwelling microwave radiation at spatial intervals from 12.5 km at 85.5 GHz to 25 km at the three lower frequencies. The sensor footprints

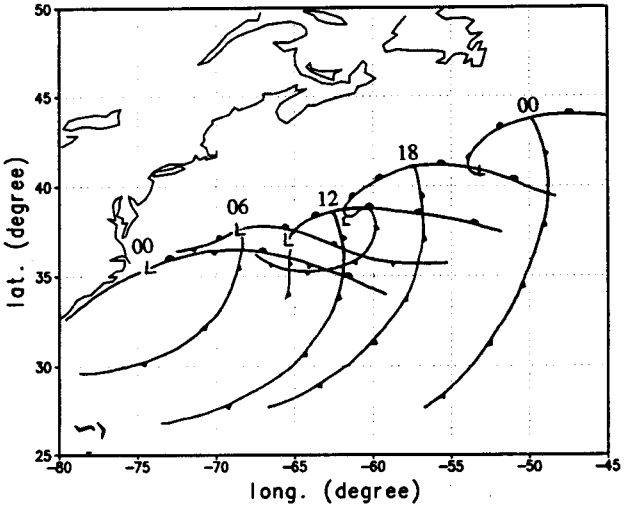


FIG. 3. (a) Surface frontal positions at 0000, 0600, 1200, and 1800 UTC 4 January and 0000 UTC 5 January 1989, based on Neiman et al. (1993). The times are written over the triple point, where the cold front intersects the warm front.

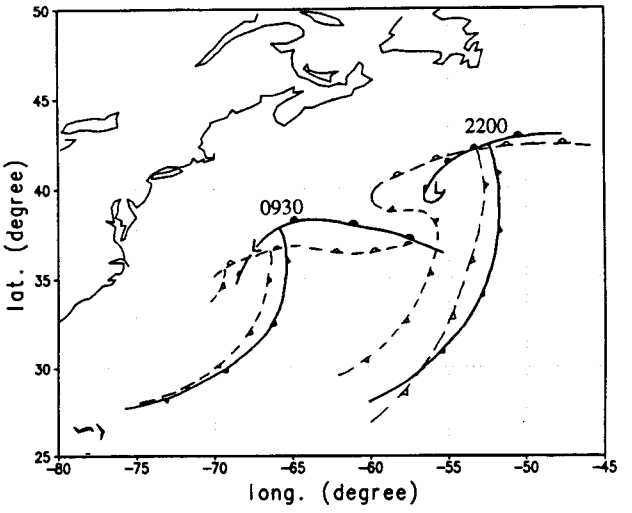


FIG. 4. Frontal positions at 0930 and 2200 UTC 4 January by a linear interpolation in time of Neiman et al. (solid lines). Numerical model-simulated frontal positions valid at 0930 and 2200 UTC are plotted in dashed lines.

range in diameter from 55 km at 19 GHz to 15 km at 85.5 GHz. More detailed SSM/I sensor description can be found in Hollinger (1989, 1991).

Several SSM/I rain-rate algorithms have been developed (Adler et al. 1991; Kummerow et al. 1989). The rain-rate algorithm used in this study was described by Olson (1989) and Hollinger (1991). Since the 85-GHz (V) channel was deemed unstable during ERICA, an alternative algorithm was applied using the 85-GHz (H) channel, as well as the 22-GHz (V), 37-GHz (V), and (H) channels and the 19-GHz (V) and (H) channels. Pixels within ±100 km of the coast were not processed, because of possible ambiguity, although additional algorithms for the land–sea interface are now being developed (Adler 1992, personal communication). The recommended alternate algorithm (Hollinger 1991) is used:

$$R = \exp(-0.42383 - 0.0082985T_{85h} + 0.01496T_{19v} + 0.00583T_{19h}) - 4.0 \text{ mm h}^{-1}, \quad (1)$$

over the ocean, and

$$R = \exp(1.32526 - 0.08150T_{37v} + 0.01638T_{37h} + 0.03561T_{22v} + 0.05079T_{19v} - 0.01875T_{19h}) - 8.0 \text{ mm h}^{-1}, \quad (2)$$

over land, where $R$ is the rainfall rate and $T_{37v}$, $T_{37h}$, $T_{19v}$, $T_{19h}$, $T_{22v}$, and $T_{85h}$ are the brightness temperatures (BT) of the 37-GHz (V), 37-GHz (H), 19-GHz (V), 19-GHz (H), 22-GHz (V), and 85-GHz (H) channels, respectively.

The SSM/I wind speed algorithm was designed to retrieve wind speeds over the oceans and to be valid

at 19.5 m above the ocean surface. The magnitude of microwave energy being emitted from the ocean surface is a function of the wave structure and foam coverage, which in turn are influenced by the wind speed. Therefore, by measuring the ocean surface microwave emission, the SSM/I is able to infer marine surface wind speeds. The 19-GHz (V) and 37-GHz (H) polarized channels are most sensitive to the ocean roughness and foam (Goodberlet et al. 1989). Two other channels, the 22 GHz (V) and 37 GHz (V), are also used to subtract from atmospheric effects in estimating a surface wind speed. The 22-GHz (V) channel is used to address atmospheric water vapor effects, while the difference between the 37-GHz (V) and 37-GHz (H) channels (37V − 37H) are used to detect cloud and liquid water scattering (Goodberlet et al. 1989). The recommended algorithm for wind speed in meters per second (WS) (Hollinger 1991) is

$$\mathrm{WS} = 147.90 + 1.0969T_{19v} - 0.4555T_{22v} - 1.7600T_{37v} + 0.7860T_{37h}, \quad (3)$$

where $T_{22v}$ are the BTs of the 22-GHz (V) polarized channel and the other variables are as before.

Upwelling microwave energy at the SSM/I frequencies emitting from the ocean surface is masked by rain and hail in the atmosphere. Additionally, the effective resolution of the algorithm is limited by the resolving power of the SSM/I antenna at 19, 22, and 37 GHz. Furthermore, the naturally presented high spatial variabilities in wind speed are smoothed, resulting effectively in a reduction of resolution. Therefore, wind speed retrieval is quite sensitive to atmospheric conditions, and "rain flags" have been established to estimate the degree of uncertainty of each calculated wind speed due to the presence of intervening water vapor, cloud water, rain, or hail (Goodberlet et al. 1989). For the least contaminated wind retrieval, flag 0, the expected error is 1 m $s^{-1}$. The errors for flags 1 and 2 are, respectively, 2–5 m $s^{-1}$ and greater than 5 m $s^{-1}$ (Hollinger 1991; Alliss et al. 1993). These latter errors are too large for meaningful analysis of the IOP 4 storm; therefore, to be conservative, the comparison in our study will be carried out only for flag 0 retrievals.

The SSM/I is also capable of measuring the amount of water vapor present between the ocean's surface and the top of the atmosphere. The IWV content of the atmosphere is important because it can provide valuable information on the location of surface fronts. Similar to the rain rate, many SSM/I water vapor algorithms have been developed (e.g., Alishouse et al. 1990). The algorithm used in this study is described in more detail in Hollinger (1991); however, it uses a nonlinear combination of the BTs from the 19-, 22-, and 37-GHz channels. The algorithm was validated by large quantities of radiosonde measurements of water vapor, and can provide IWV values from 0 to 80 kg $m^{-2}$ (or 8-cm equivalent depth of water).

SSM/I observations of the ERICA IOP 4 cyclone were available at 0000, 0930, and 2200 UTC 4 January during the period between 0000 UTC 4 January and 0000 UTC 5 January. Brightness temperatures were sampled at a resolution of 25 km in longitude and latitude for the precipitation and approximately 50 km for both the IWV and marine wind speeds. All retrieved fields are then bilinearly interpolated to a grid with 0.25° resolution in latitude and longitude, covering the same domain as the Naval Research Laboratory (NRL) numerical model. Missing pixels within the swath were given values equal to the average value of surrounding pixels. A five-point running average was performed on most of the SSM/I fields, which will be discussed, unless specified otherwise. Because the cyclogenesis of the IOP 4 storm occurred almost entirely over the ocean, and the greater uncertainties of retrieval over land, only observations over the ocean in SSM/I swaths are discussed.

## 4. Numerical model

The model used for this study is the NRL limited-area numerical weather prediction system. The system contains an objective analysis scheme, initialization, the numerical model, and the output–diagnostics package. The numerical model is a three-dimensional, hydrostatic, primitive equation system that includes planetary boundary layer (PBL), cumulus, and radiation parameterizations. The formulation of the model is described in Madala et al. (1987), Chang et al. (1989), and Holt et al. (1990).

The version of the model that generated the result for the comparison in this study is identical to the one in Chang and Holt (1993) and Chang et al. (1993). The model contains 136 × 141 horizontal grid points with a horizontal resolution of 0.33° in longitude and 0.25° in latitude. The horizontal resolution is designed to have nearly the same effective resolution of the SSM/I measurements. The model domain covers the east coast of the United States and the western North Atlantic from 20° to 55°N and 85° to 40°W. This version of the model has 16 sigma layers in the vertical.

The PBL parameterization is based on the budget equations of the turbulent kinetic energy (TKE) and dissipation rate. A soil slab model is used to forecast the land surface temperature. The ERICA data center's 50-km resolution sea surface temperature dataset is used to describe the sea surface temperature. The 50-km dataset is used because it shows a strong gradient between the Gulf Stream and the continental shelf/slope water. A modified Kuo cumulus parameterization is used. The model uses the NMC RAFS 2.5° analysis at 0000 UTC 4 January as the initial conditions for the integrations. The RAFS analysis is not enhanced by the SSM/I observations. Therefore, the simulated storm behavior and structures can be considered independent of the SSM/I-observed fields.

The simulated fronts at SSM/I overpasses of 0930 and 2200 UTC, subjectively determined based on simulated mass and momentum fields, are depicted in Fig. 4. As shown in Chang and Holt (1993), the model-simulated minimum sea level pressure (SLP) of the ERICA IOP 4 storm starts from 998 mb at 0000 UTC 4 January and deepens to 952 mb in 24 h, an underprediction of the intensification by 15 mb. However, it is not the purpose of this study to reproduce the remarkable intensification of the IOP 4 cyclone. Model-simulated results are used in this study to mainly fill in the gap in time and space between the SSM/I overpasses at 0930 and 2200 UTC 4 January. The model produces high resolution (compared to available conventional observations) and dynamically consistent mass and momentum fields that give a more complete view of the cyclone and associated fronts than may be possible using the relative narrow SSM/I swath of 1400 km. Also, model-simulated IWV and precipitation rates provide reasonable comparisons with SSM/I retrievals that are not available from conventional observations. As will be discussed, the model-simulated storm track is approximately 1°–2° latitude south of the analyzed track. Therefore, when model results are compared with observations and SSM/I retrievals, it is constructive to discuss the simulated fields relative to the simulated cyclone and frontal positions.

## 5. 0000 UTC 4 January

### *a. Rain rate*

At 0000 UTC 4 January, a weak surface disturbance started to organize off the East Coast as two upper-level short-wave troughs were merging. The cold front structure and convective activities were not yet prominent, as indicated by the *GOES-7* IR image (Fig. 5). The SSM/I pass at 0000 UTC showed an area of light precipitation from the coastal waters off southern Virginia and south along the North and South Carolina coastlines (Fig. 6). The areas of heavier precipitation were oriented northeast–southwest along the Gulf Stream, with maximum rainfall rates of 9 mm $h^{-1}$. Although there was little organization of the precipitation pattern with respect to the developing cyclone at 0000 UTC as the storm was in its initial stage, the SSM/I-observed heavier precipitation bands are parallel to the front analyzed by Neiman et al. (1992), as was the GOES imagery (Fig. 5). The orientation of the bands also appears to be parallel to the coast and to the sea surface temperature, suggesting that the air–sea–land interaction may have affected the organization of the convections at the early stage of the cyclogenesis. The gap in the convective activity along the front was evident in both the IR and SSM/I images.

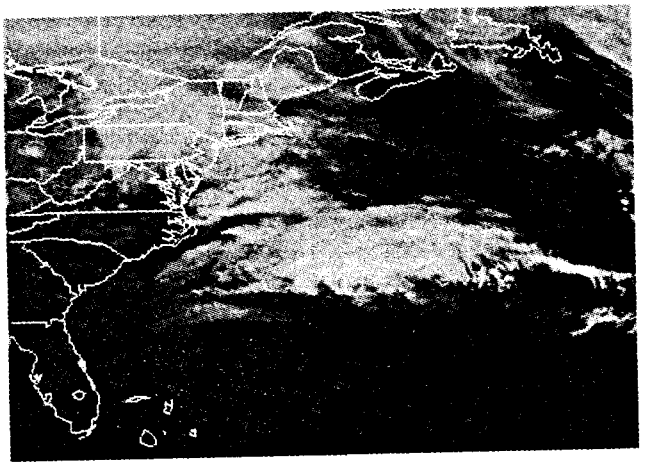

FIG. 5. *GOES-7* enhanced IR image at 0000 UTC 4 January.

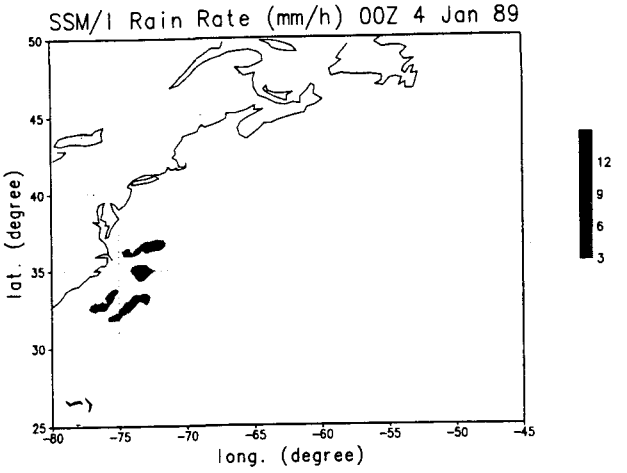


FIG. 6. SSM/I rainfall rates (mm $h^{-1}$) at 0000 UTC 4 January. The intensity of precipitation for all rain-rate figures is indicated by the gray scales on the right.

### *b. IWV*

Figure 7 shows the SSM/I IWV pattern at 0000 UTC 4 January, with the surface stationary front as analyzed by Neiman and Shapiro (1993) superimposed. The strongest IWV gradient was found in the cold-air sector of the storm. The sharpest gradient of SSM/I IWV occurred along the Carolina coast, probably due to the sea–land contrast and the Gulf Stream. Some considerable gradient also existed to the north of the analyzed front east of the Virginia shoreline, also likely to be modulated by the sea surface temperature (SST) distribution there. In a study of North Pacific winter cyclones using microwave data from the *Nimbus-7* satellite, Katsaros and Lewis (1986) found that a strong gradient in integrated atmospheric water vapor was a good indicator for locations of surface fronts. These results were further supported by similar studies described in Katsaros et al. (1989) and McMurdie and Katsaros (1985). Here, the surface cold and warm

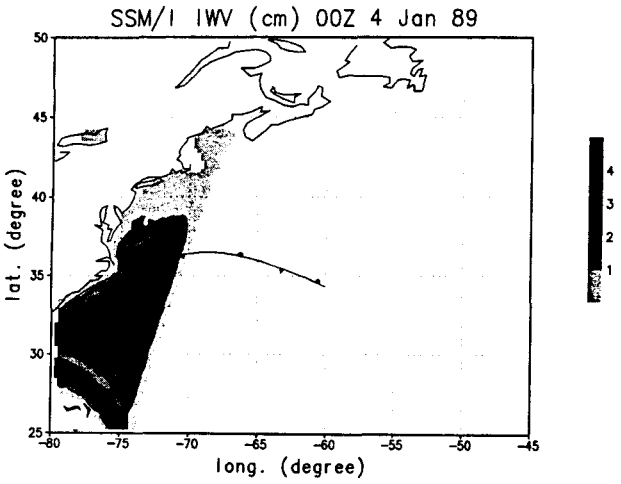


FIG. 7. SSM/I-retrieved integrated water vapor (cm) equivalent water depth at 0000 UTC 4 January with analyzed front. Front analyzed by Neiman et al. is superimposed.

fronts were located just west and north, respectively, of the maximum IWV. Values greater than 32 mm were common in the warm sector, with maximums greater than or equal to 40 mm occurring near the Gulf Stream. In contrast to the Neiman and Shapiro analysis (Fig. 7), the NMC surface analysis (not shown) placed the cold front west of the low center in a concave curvature, more in agreement with the IWV gradients.

### c. *Surface wind speed*

Figure 8 shows the SSM/I-retrieved marine surface wind speeds at 0000 UTC 4 January, plotted as isotachs at a 3 m $s^{-1}$ interval. Only wind retrievals with flag = 0 were plotted. Unfortunately, areas of high wind near the center of the low pressure center were under cloud cover (Figs. 5 and 6), rendering wind speed retrievals highly unreliable near the low center. Several ship- and buoy-reported wind bars taken from Sanders surface analysis were also plotted for comparison. The three reports north of 37°N seemed to agree well with the SSM/I retrievals. The report just offshore of 2.5 m $s^{-1}$ wind was located in a region where SSM/I retrievals showed 0–3 m $s^{-1}$. The two other reports of 5 m $s^{-1}$ were in an area where SSM/I retrieved 3–6 m $s^{-1}$.

In the small region just offshore of North Carolina, the SSM/I-retrieved wind speeds of more than 12 m $s^{-1}$ were supported by the 17.5 m $s^{-1}$ wind reported by a nearby ship *WRGL*, although it could not be ascertained whether the ship was within the area of higher retrieval uncertainties (i.e., flag greater than zero). The two reports of 10 and 12.5 m $s^{-1}$ south of 30°N seemed to be 1–2 m $s^{-1}$ higher than the SSM/I retrievals. These errors are within the expected range of the SSM/I calibration and validation (Hollinger 1991).

## 6. 0930 UTC 4 January

### a. *Rain rate*

At 0930 UTC 4 January, the IOP 4 cyclone was well developed, with a minimum SLP of 970 mb (Sanders analysis). The *GOES-7* enhanced IR image (Fig. 9) showed a well-developed comma-shaped cloud pattern with very cold cloud tops near 40°N, 65°W, just northeast of the analyzed triple point (the intersection of the warm and cold front). High clouds were also evident along the tail of the comma-shaped cloud pattern. These high cloud tops were located mostly east of 65°W, well to the east of the analyzed cold front. The frontal system (Fig. 4) showed an occluded warm front (Neiman et al. 1993) with a "T-bone" shape structure (Shapiro and Keyser 1990). Figure 10a shows the SSM/I-retrieved precipitation-rate pattern at 0930 UTC with the interpolated frontal position [Neiman and Shapiro (1993) analysis]. This overpass captured only a portion of the storm's precipitation field and missed the low center. Significant retrieved rainfall occurred in association with both the interpolated cold and warm fronts and primarily in the warm sector, with the heaviest precipitation (rates greater than 12 mm $h^{-1}$) located just to the east of the triple point. The SSM/I precipitation was mostly prefrontal near the interpolated cold front. Along the warm front, the heavy precipitation shifted from prefrontal near the triple point to postfrontal toward the east. This shifting was also recognizable from Fig. 2 of Wakimoto et al. (1992); it showed the GOES infrared imagery and frontal positions at 0600 UTC.

Figure 10b shows the NRL model-simulated sea level pressure (SLP) and precipitation-rate fields at 9.5 h, valid for 0930 UTC 4 January. Superimposed on Fig. 10b was the model-produced fronts based on simulated

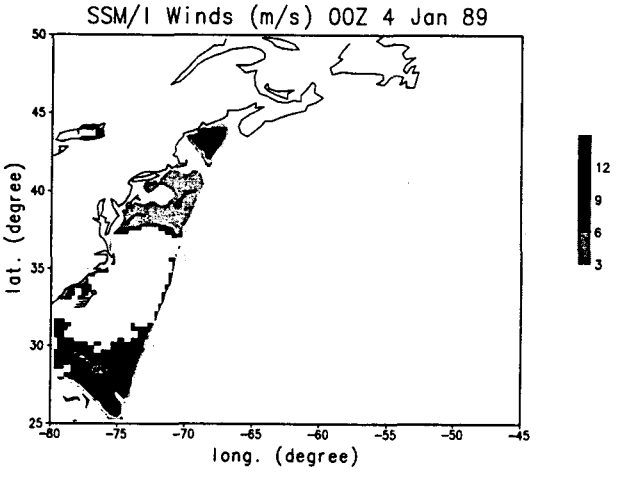


FIG. 8. SSM/I-retrieved marine surface wind speeds with flag 0. Ship and buoy reports are superimposed with half-barbs of 2.5 m $s^{-1}$, barbs of 5 m $s^{-1}$, and flags of 25 m $s^{-1}$.

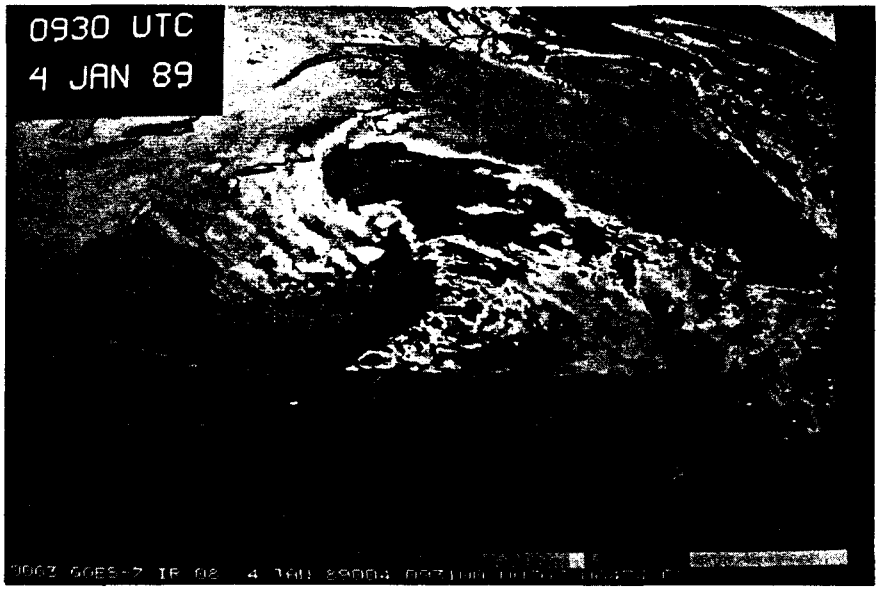


FIG. 9. *GOES-7* enhanced IR image at 0900 UTC 4 January.

mass and momentum fields. [More detailed discussion of the model cyclone and frontal structure will be reported in Chang et al. (1993).] Model-simulated precipitation over the cyclone scale had already developed a comma-shaped pattern, but there was very little precipitation at the low pressure center. Model-produced heaviest precipitations concentrated mostly along the warm front. A maximum rainfall rate of 17 mm $h^{-1}$ was predicted just to the north of the low center, where there was a hook-shaped convective pattern, as observed at 0600 UTC (Figs. 1 and 2 in Wakimoto et al.). To the east of the triple point, the precipitation shifted to the south of the warm front, similar to the relative position of the SSM/I precipitation and the analyzed (interpolated) fronts of Neiman and Shapiro. Unfortunately, because the SSM/I swath at 0930 UTC just missed the low center, a comparison of the precipitation patterns near the center could not be made. The model-produced warm front, lying to the west of the triple point, started to bend back toward the south at this time due to the strong cross-frontal shear. This was coincident with the westward development of the low pressure center along the occluded warm front. Along the cold front there was a band of light precipitation. Around the western tip of the low center, a secondary push of cold air was evident in the rainfall-

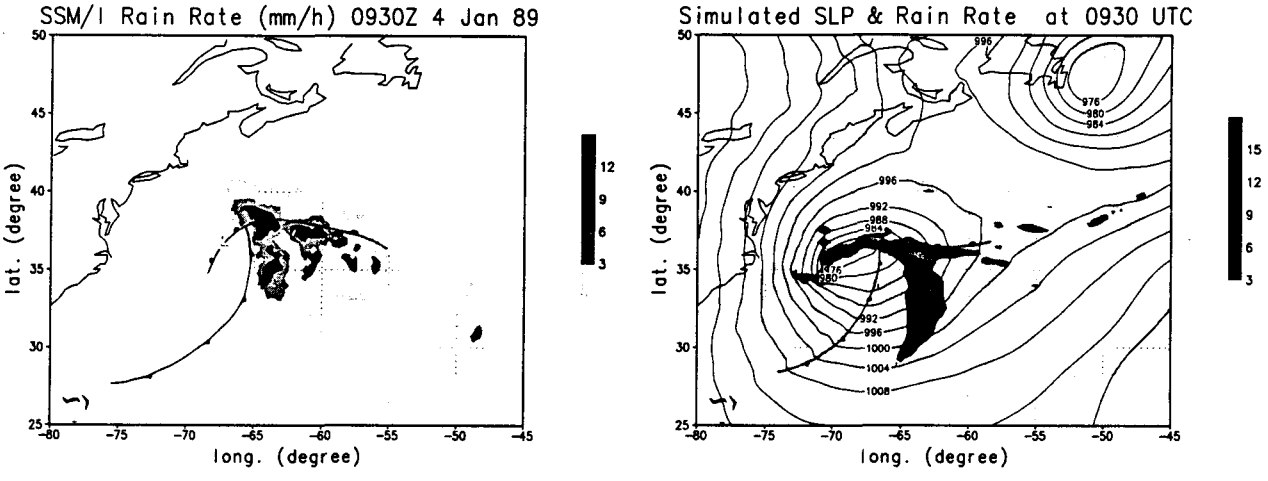


FIG. 10. (a) SSM/I rainfall rates at 0930 UTC, with the interpolated analyzed frontal position superimposed. (b) Model-simulated SLP (mb, isobars in solid lines, 4-mb intervals) and rainfall rate (mm $h^{-1}$, in shades) at 9.5 h, valid for 0930 UTC 4 January, with simulated frontal position superimposed.

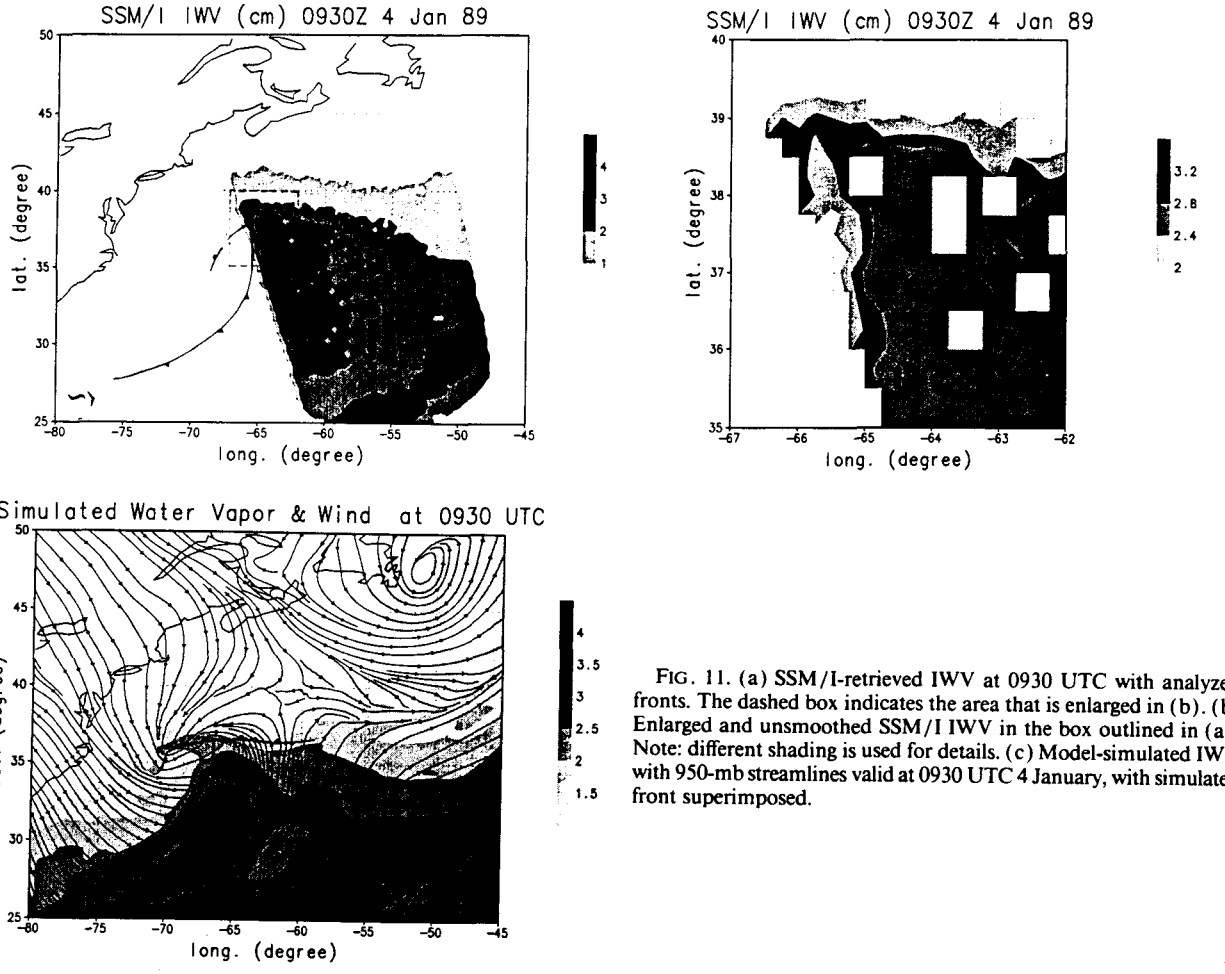


FIG. 11. (a) SSM/I-retrieved IWV at 0930 UTC with analyzed fronts. The dashed box indicates the area that is enlarged in (b). (b) Enlarged and unsmoothed SSM/I IWV in the box outlined in (a). Note: different shading is used for details. (c) Model-simulated IWV with 950-mb streamlines valid at 0930 UTC 4 January, with simulated front superimposed.

rate pattern and in the IWV, which is discussed in the following. The north–south-oriented precipitation along 63°W was displaced several hundred kilometers east of the cold front. The IR imagery at 0600 (see Wakimoto et al. 1992) and 0930 UTC in Fig. 9 also suggested a strong convection band well east of the cold front. In all, the SSM/I-retrieved precipitation pattern seemed to agree with the model-produced pattern within the SSM/I swath. However, the model produced heavier (lighter) precipitation along the warm (cold) front compared to the retrieval.

*b. IWV*

Figure 11a shows the SSM/I-retrieved IWV pattern at 0930 UTC along with the interpolated Neiman et al. frontal analysis. The pattern showed high IWV values (>3 cm) in the warm sector, with a band of extremely high moisture (IWV > 4 cm) located just to the east of the cold front. Strong IWV gradients existed to the north of the warm front. The interpolated warm front nearly coincided with the 3-cm contour, giving credence to the assertion of Katsaros and Lewis (1986) that the strong IWV gradient was a good indicator of the surface front. To the southeast and away from the IOP 4 cyclone, there was another high IWV between 30°N, 50°W and 25°N, 55°W.

Because the low center was located just outside of the SSM/I swath, and the triple point just inside, the box encircled by the dashed lines in Fig. 11a between 35°–40°N and 67–62°W deserved an enlargement for a detailed view. The enlarged SSM/I-retrieved IWV field shown in Fig. 11b was not smoothed, and missing pixels (white squares in the swath) were not filled in. In Fig. 11b, the warm front was clearly located along the 3-cm IWV contour between 38° and 39°N. There was no discernible discontinuity of IWV on the north side of the warm front at the triple point, characteristic of a warm front occlusion. The cold front was also along the 3-cm contour just west of 65°W. West of the advancing cold front there was a notch of dry air along the western edge of the swath where the IWV decreased to 2 cm, most noticeable at 37.5°N, 65.5°W. This was an indication of the wraparound of cold and dry air, transported by the southwesterly flow behind the cold front. The intrusion of the cold and dry air to the south

and east of the low center was also evident from the model-simulated IWV field (Fig. 11c). The westward extension of the high IWV north of the low center and the eastward extension of the low IWV south of the low center depicted the circulation around the occluded warm front. Strong IWV gradients were located to the north of the warm front and to the west of the cold front. Compared to the SSM/I IWV, the model-produced IWV was approximately 0.5 cm lower. Along the warm front, the 2.5-cm contour was north of the warm front west of the triple point but gradually shifted to south of the warm front farther east, consistent with the simulated precipitation pattern (Fig. 10b). The warm sector had high IWV values with two very high IWV bands extended from the tropics at 70° and 60°W, outlining the conveyor belts of moisture supply from low latitudes into the marine cyclone. In general, SSM/I-retrieved and model-produced IWV fields agreed very well relative to their respective (analyzed and simulated) frontal positions.

### c. *Surface wind speed*

The SSM/I-retrieved surface winds at 0930 UTC are depicted in Fig. 12. Again, the high wind area near the low center and frontal regions were excluded due to high uncertainties (flag numbers greater than zero). For comparison, selected ship reports at 0600 (denoted by black dots) and 1200 (denoted by open circles) UTC outside the cloud shields were plotted. There was a rapid wind shift north of 40°N due to the departure of a previous cyclone and the approaching of the IOP 4 storm (Fig. 10b). In this region, SSM/I-retrieved wind speeds seemed to be consistently 1–4 m $s^{-1}$ lower than the ship reports. Counting clockwise from the report near 40°N, 50°W, the ship-reported and -retrieved wind speeds were 15 versus 12–15 m $s^{-1}$, 12.5 versus 9–12 m $s^{-1}$, 10 versus 6–9 m $s^{-1}$, 5 versus 6–9 m $s^{-1}$, 10 versus 6–9 m $s^{-1}$, 5 versus 3–6 m $s^{-1}$, and, finally, 10 versus 3–6 m $s^{-1}$. To the south of the cloud shield in the warm sector where the southwesterly winds were steady the agreement between the SSM/I retrieval and ship reports was very good. This suggests that the steadiness of marine boundary layer winds and ocean surface wave characteristics must be taken into consideration in designing a surface wind algorithm in the future to achieve higher accuracy.

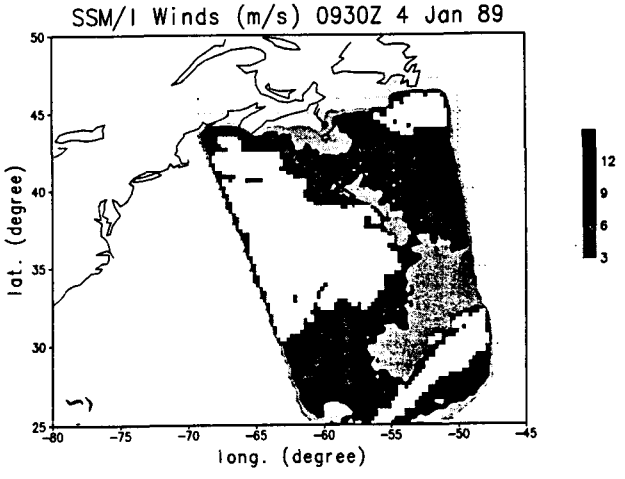


FIG. 12. Same as Fig. 8—SSM/I-retrieved marine surface winds with flag 0 except at 0930 UTC. The ship reports with black dots are at 0600 UTC—with open circles, at 1200 UTC.

## 7. 2200 UTC 4 January

### a. *Rain rate*

At 2200 UTC, the IOP 4 cyclone had experienced the most rapid intensifying stage, reaching a central SLP of about 940 mb, close to the lowest SLP of the system. The cyclone was almost in the middle of the Atlantic Ocean, and the comma-shaped cloud seemed to occupy much of the basin. The GOES enhanced IR (Fig. 13) showed a convectively active band extended from the north of the low center, arcing around the east and south perimeter. High clouds extended into the Gulf of St. Lawrence. The cold and drier air had intruded near the low center as indicated by the partial clearing near the center. Disorganized shallow convections dominated in the cold air mass behind the cold front along 35°N and between 70° and 55°W where significant air–sea heat transfers occurred (Atlas et al. 1986). The system would deepen only a few millibars more, and the overall convective activity started to weaken. The SSM/I swath encompassed most of the cold front (Fig. 14). There was almost no heavy precipitation around the low center. The rain rate showed that there were many mesoscale active convections, with a rain rate greater than 12 mm $h^{-1}$ embedded along the cold front, as evident in the IR imagery (Fig. 13) and radar observations (Wakimoto et al. 1992). One particular interesting feature in Fig. 14 was that the heavier precipitation was displaced to the east along the northern portion of the cold front but was consistent with the southern portion of the cold front. This was similar to what Wakimoto et al. had found at 1800 UTC (Fig. 7c of their paper), although the convection–front intersection point at 2200 UTC was closer to the warm front than at 1800 UTC. This could mean 1) that the Neiman et al. analyzed cold front was misplaced, or 2) that the displacement between the convection and cold front existed throughout the evolution of the cyclone.

The 22-h model-simulated rainfall rate, valid for 2200 UTC, was shown in Fig. 14b. The low pressure center was now almost devoid of precipitation. The precipitation pattern near the center obtained an eyewall-like shape, similar to the IR image (Fig. 13). Major precipitation occurred along the warm front and extended from the triple point at approximately 41°N

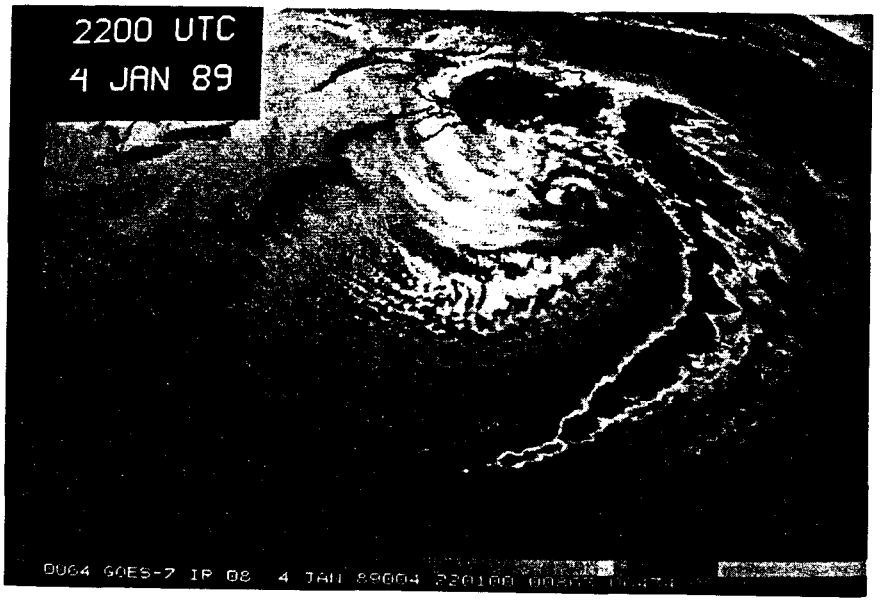


FIG. 13. *GOES-7* IR imagery at 2200 UTC 4 January.

along the cold front to 25°N. The simulated rain-rate distribution clearly depicted the right-angled intersection of the cold front to the warm front. Simulated mass and momentum fields seemed to support the existence of the secondary cold front analyzed by Sanders and Neiman et al. The model-simulated temperature gradient was situated behind the secondary cold front. The primary cold front had little temperature gradient associated with it. In fact, there was warm advection across the primary cold front. Between the primary "cold" front and the secondary cold front there was a relatively cloud-free zone. To the west of the secondary cold front and in the cold air there were scattered and disorganized convection, consistent with the GOES IR image (Fig. 13). (A more detailed description of model results will be reported in Chang et al. 1993.) Compared to the SSM/I-retrieved rain rates, the model produced heavier precipitation along the warm front, with a maximum rate of 20 mm $h^{-1}$, and lighter precipitation along the cold front, with a maximum rate of 3 mm $h^{-1}$. The squall-line feature east of the primary cold front was evident in the model simulation, enhanced IR, and SSM/I retrieval.

### *b. IWV*

SSM/I-measured IWV at 2200 UTC is shown with an interpolated front in Fig. 15a. The area with more

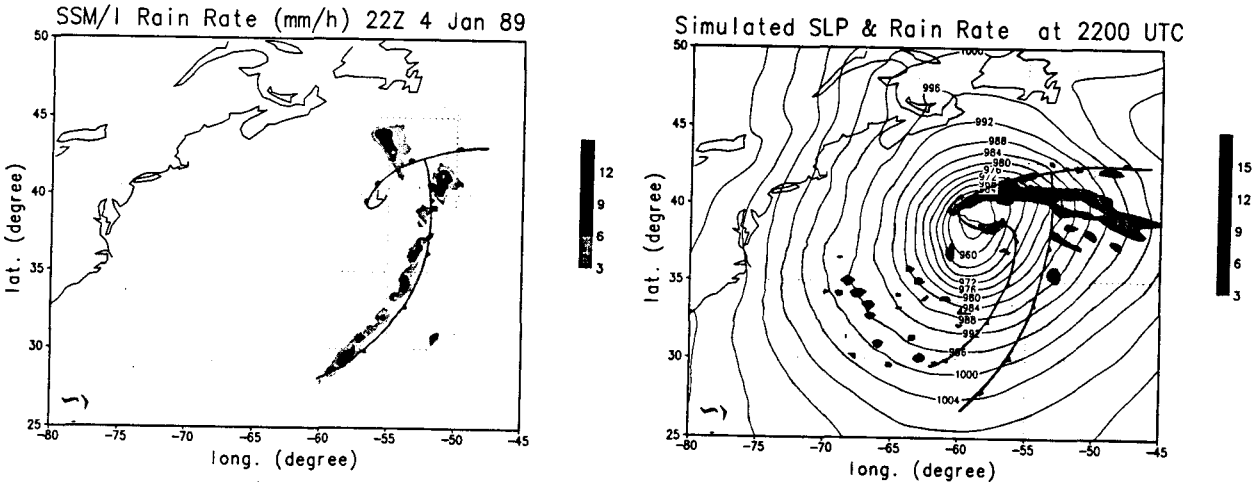


FIG. 14. (a) Same as Fig. 10a except for 2200 UTC 4 January. (b) Same as Fig. 10b except for 2200 UTC 4 January.

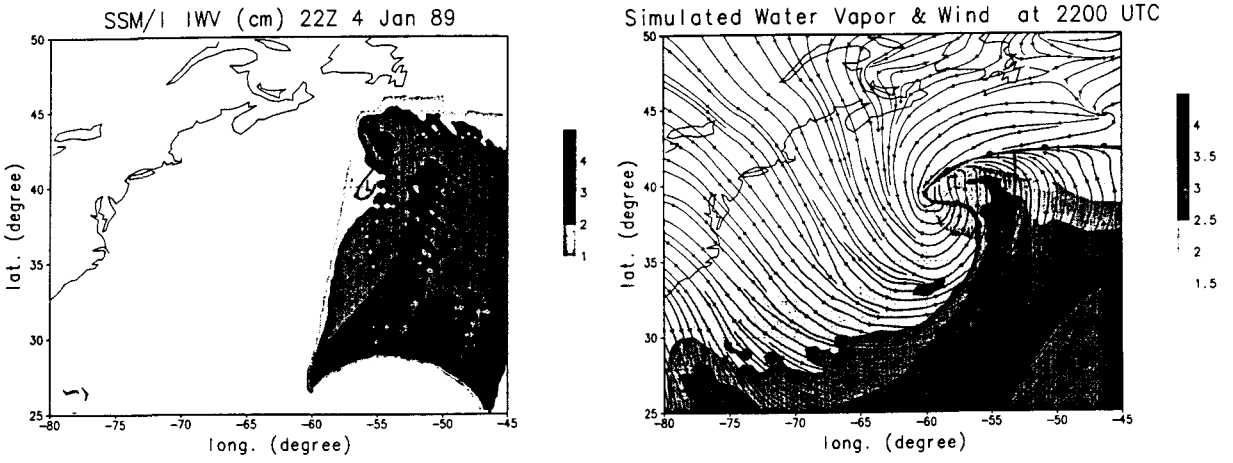


FIG. 15. (a) Same as Fig. 11a except for 2200 UTC 4 January. (b) Same as Fig. 11c except for 2200 UTC 4 January.

than 3 cm of IWV had extended farther north together with the warm sector compared to 0930 UTC (Fig. 11a). The interpolated cold front now was located mostly to the east of the 3–4-cm contour in agreement with the location of the SSM/I-observed precipitation west of the cold front. There was an isolated area with IWV > 3 cm north of the occluded warm front, collocated with the heavy precipitation there (Fig. 14).

Figure 15b shows the model-simulated IWV and 950-mb streamlines valid for 2200 UTC. Similar to the IWV field at 0930 UTC (Fig. 11c), the high IWV values were found mostly in the warm sector. A moist tongue extended from the tropics just ahead of the primary cold front to the high latitudes and to the east of the storm. In the cold air, IWV decreased rapidly toward the west, in spite of the long fetch over warm ocean. Strong gradients again were located along the warm and cold fronts. The model-simulated primary cold front was more associated with IWV gradients than with temperature gradients (see section 6a). Distribution of IWV near the center still reflected the effect of horizontal advection by the frontal and cyclonic circulations. The circular area with relative low IWV at 39°N, 57°W was collocated with the precipitation-free area between the two eyewall-like regions of convection. The high IWV band east of the cold front in the simulation was in agreement with the aforementioned squall-line feature. Overall, the model-simulated IWV values were less than the SSM/I retrieved by no more than 0.5 cm.

### c. *Surface wind speed*

Cloud cover and high wind speeds at this time rendered most wind retrievals unreliable (flag greater than zero) over most of the swath (Fig. 16). The comparison of the retrieved with the two ship reports near the storm center with 30 and 40 m $s^{-1}$ wind was not meaningful due to the uncertainty of the locations. One report of 12.5 m $s^{-1}$ within the swath east of 50°W was in an area of 6–9 m $s^{-1}$ retrieved speed. This showed the limitation of the SSM/I marine surface wind retrieval. Continuous vigorous validation with wind speeds over 12 m $s^{-1}$ can perhaps improve the confidence level of flag 1 retrievals. We found that for this particular storm, the area cover by high flags (>0) coincides approximately with the gale force wind region. The boundary of the high flag region may well be used for gale-force warning; however, the generalization to other cases cannot be made.

## 8. Conclusions

Patterns of rainfall rates, integrated water vapor and marine surface wind speeds were derived from SSM/I brightness temperatures. These fields were used to analyze the explosive midlatitude cyclone that developed during ERICA IOP 4. In addition, the SSM/I fields were compared to in situ ship and buoy

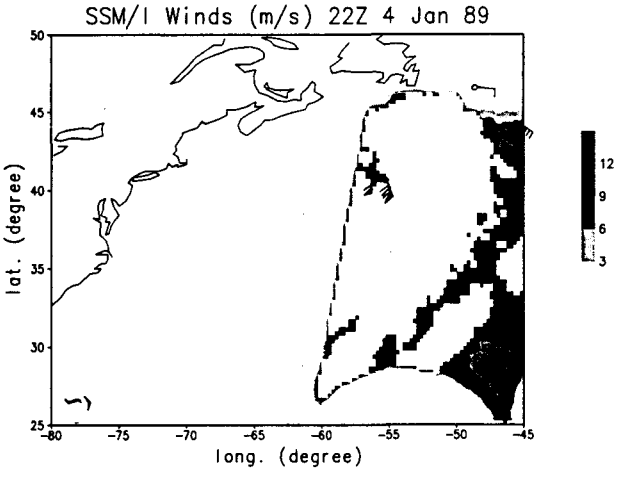


FIG. 16. Same as Fig. 12 except at 2200 UTC 4 January. Black dots denote reports made at 1800 UTC 4 January—open circles, at 0000 UTC 5 January.

reports and to results produced by the NRL limited-area model.

This study has determined that SSM/I-derived rainfall rates were found along and ahead of the cold and warm fronts during the mature stage of the storm. These results also supported those shown by the model simulations. The active warm front and the warm-front occlusion (the "T-bone" fronts) in the Neiman and Shapiro (1993) surface analysis were evident in the SSM/I-observed precipitation patterns. Mesoscale areas of convection observed by SSM/I along the cold front supported the precipitation field observed by airborne radar (Wakimoto 1992). Additionally, the increase in areal coverage and intensity of SSM/I rainfall rates was consistent with the observed intensification of the storm. Quantitative comparison with model simulated rainfall rates was made. In general, the model simulated rainfall rates along the warm front were higher by a maximum of 5 mm $h^{-1}$, and rainfall rates along the cold front were lower by a maximum of 3–5 mm $h^{-1}$.

Patterns of SSM/I-derived IWV were viewed. It was found that the IWV had the strongest gradients along fronts, and the highest IWV values lay ahead of the cold front in the warm sector of the storm. Values in excess of 40 mm were not uncommon within the warm sector of this storm. The IWV patterns can provide additional information for frontal analysis, especially over regions where conventional data are sparse or a cirrus shield is particularly dense. The pattern of the SSM/I-retrieved IWV fields on the cyclone scale and frontal scale were further supported by NRL limited-area model forecasts. SSM/I-retrieved IWV values were generally 5 mm higher than model-simulated values.

Compared with ship reports, the SSM/I-retrieved marine surface wind speeds were slightly lower by 1–3 m $s^{-1}$. However, in regions of rapid wind shifts, as we found in the case of 0930 UTC overpass, the difference was larger. The IOP 4 storm, because of its location (over the ocean), size, and intensity, provided an excellent opportunity to apply the SSM/I wind speed algorithm in determining the boundary of near-gale force winds (15 m $s^{-1}$).

The potential usefulness of the SSM/I instrument in the analysis of midlatitude cyclones has been addressed. Because of its better resolution, SSM/I-retrieved IWV and precipitation patterns are very useful in supplementing conventional data in subjective analyses, especially for weather systems over data-sparse oceans. The rainfall rate, IWV, and marine surface wind speeds can also be very beneficial in objective analysis and numerical weather predictions. Marine surface wind speeds are being used in global data assimilations at NMC (Yu and Deaven 1991) and Fleet Numerical Ocean Center (Goerss and Phoebus 1992). Chang and Holt (1993) discussed the methodology and demonstrated the potential benefit of assimilation of SSM/I rainfall rates in a limited-area numerical model. The rainfall rate can be used in dynamic initializations as well as in forecast models as forcing functions. The IWV can be used in moisture analysis or can provide surface latent heat fluxes (Miller and Katsaros 1992). Further exploitation and applications of SSM/I-retrieved fields are being conducted at NRL.

*Acknowledgments.* We thank Dr. James Hollinger, Mr. Glenn Sandlin, and Mr. David Spangler of the Naval Research Laboratory for providing the SSM/I data. We thank Dr. Paul Neiman for sending us his yet unpublished manuscripts on the ERICA IOP 4 cyclone. We also thank Prof. Fred Sanders for sending us his surface analysis. His interest and comments, and those from four anonymous reviewers, have greatly improved the presentation of our paper. The research was supported by an NRL basic research fund and an ONR Grant N00014 92 AF002.

## REFERENCES

Adler, R. F., H.-Y. M. Yeh, N. Prasad, W.-K. Tao, and J. Simpson, 1991: Microwave simulation of a tropical rainfall system with a three-dimensional cloud model. *J. Appl. Meteor.*, **30,** 924–953.

Alishouse, J., S. Snyder, J. Vongsathorn, and R. Ferraro, 1990: Determinations of oceanic total precipitable water from the SSM/I, *IEEE Trans. Geosci. Remote Sens.*, **28,** 811–816.

Alliss, R. A., S. Raman, and S. W. Chang, 1992: Special Sensor Microwave/Imager (SSM/I) observations of Hurricane Hugo (1989). *Mon. Wea. Rev.*, **120,** 2723–2737.

——, S. W. Chang, and S. Raman, 1993: Applications of SSM/I data in the analysis of Hurricane Florence (1988). *J. Appl. Meteor.*, **32,** in press.

Atlas, D., B. Walter, S. Chou, and P. J. Sheu, 1986: The structure of the unstable Marine boundary layer viewed by lidar and aircraft observations. *J. Atmos. Sci.*, **43,** 1301–1308.

Chang, S. W., and T. R. Holt, 1993: Impact of SSM/I rainfall rates on numerical predictions of winter cyclones. *Mon. Wea. Rev.*, **121,** in press.

——, K. D. Sashegyi, and T. R. Holt, 1991: Important physical processes in the evolution of mesoscale frontal structure of the ERICA IOP-4 cyclone, *Proc., Ninth Conf. on Numerical Weather Prediction,* Denver, CO, 760–761.

——, T. R. Holt, and K. D. Sashegyi, 1993: A numerical study of the frontal structure of the ERICA IOP 4 marine cyclone. *Mon. Wea. Rev.*, **121,** in press.

——, K. Brehme, R. V. Madala, and K. D. Sashegyi, 1989: A numerical study of the East Coast snowstorm of 10–12 February 1983. *Mon. Wea. Rev.*, **117,** 1768–1778.

Georss, J. S., and P. A. Phoebus, 1992: The navy's operational atmospheric analysis. *Wea. Forecasting,* **7,** 232–249.

Goodberlet, M. A., C. T. Swift, and J. C. Wilkerson, 1989: Remote sensing of ocean surface winds with the Special Sensor Microwave/Imager. *J. Geophys. Res.*, **94,** 547–555.

Hollinger, J. P., 1989: DMSP Special Sensor Microwave/Imager calibration/validation, Final Report Vol. I. [Available from the author at Naval Research Laboratory, Washington, D.C. 20375.]

——, 1991: DMSP Special Sensor Microwave/Imager calibration/validation, Final Report Vol. II. [Available from the author at Naval Research Laboratory, Washington, D.C. 20375.]

Holt, T., S. W. Chang, and S. Raman, 1990: A numerical study of the coastal cyclogenesis in GALE IOP 2: Sensitivity to PBL parameterization. *Mon. Wea. Rev.*, **118,** 234–257.

Katsaros, K. B., and R. Lewis, 1986: Mesoscale and synoptic scale features of North Pacific weather systems observed with the

scanning multichannel microwave radiometer on *Nimbus 7*. *J. Geophys. Sci.*, **91**, 2321–2330.

——, I. Bhatti, L. A. McMurdie, and G. W. Petty, 1989: Identification of atmospheric fronts over the ocean with microwave measurements of water vapor and rain. *Wea. Forecasting*, **4**, 449–460.

Kummerow, C., R. A. Mack, and I. M. Hakkarinen, 1989: A self-consistency approach to improve microwave rainfall rate estimation from space. *J. Appl. Meteor.*, **28**, 869–884.

McMurdie, L. A., and K. B. Katsaros, 1985: Atmospheric water distribution in a mid-latitude cyclone observed by the Seasat scanning multichannel microwave radiometer. *Mon. Wea. Rev.*, **113**, 584–598.

——, and K. Katsaros, 1992: Satellite derived integrated water vapor and rain intensity patterns: Indicators of rapid cyclogenesis. *Proc. Sixth Conf. on Satellite Meteorology and Oceanography*, Atlanta, GA, Amer. Meteor. Soc., J11–J114.

——, G. Levy, and K. Katsaros, 1987: On the relationship between scatterometer-derived convergences and atmospheric moisture. *Mon. Wea. Rev.*, **115**, 1281–1294.

Madala, R. V., S. W. Chang, U. C. Mohanty, S. C. Madan, R. K. Paliwal, V. B. Sarin, T. Holt, and S. Raman, 1987: Description of Naval Research Laboratory limited area dynamical weather prediction model. NRL Tech. Rep. 5992, Washington, D.C., 131 pp.

Miller, D. K., and K. B. Katsaros, 1992: Satellite-derived surface latent heat fluxes in a rapidly intensifying marine cyclone. *Mon. Wea. Rev.*, **120**, 1093–1107.

Neiman, P. J., and M. A. Shapiro, 1993: The life cycle of an extratropical marine cyclone. Part I: Frontal-cyclone evolution and thermodynamic air–sea interaction. *Mon. Wea. Rev.*, **121**, 2153–2176.

——, ——, and L. S. Fedor, 1993: The life cycle of an extratropical marine cyclone. Part II: Mesoscale structure and diagnostics. *Mon. Wea. Rev.*, **121**, 2177–2199.

Olson, W. S., 1989: Physical retrieval of rainfall rates over the ocean by multispectral microwave radiometry-application to tropical cyclones. *J. Geophys. Res.*, **94**, 2267–2280.

Pudykiewicz, J., R. Beniot, and J. Mailhot, 1992: Inclusion and verification of a predictive cloud-water scheme in a regional numerical weather prediction model. *Mon. Wea. Rev.*, **120**, 612–626.

Raustein, E., H. Sundqvist, and K. B. Katsaros, 1991: Quantitative comparison between simulated cloudiness and clouds objectively derived from satellite data. *Tellus*, **43A**, 306–320.

Rodgers, E. B., and R. F. Adler, 1981: Tropical cyclone rainfall characteristics as determined from a satellite passive microwave radiometer. *Mon. Wea. Rev.*, **109**, 506–521.

Sanders, F., 1989: *Surface Analyses during ERICA*. [Available from ERICA Data Center, Drexel University, Philadelphia, PA 19104.]

Wakimoto, R. M., W. Blier, and C. Liu, 1992: The frontal structure of an explosive oceanic cyclone: Airborne radar observations of ERICA IOP 4. *Mon. Wea. Rev.*, **120**, 1135–1155.

Yu, T.-W., and D. G. Deaven, 1991: Use of SSM/I wind speed in NMC's GDAS. *Proc. 9th Conf. Numerical Weather Predictions*, Denver, CO, Amer. Meteor. Soc., 416–417.